Measurement report: Vertical profiling of particle size distributions over Lhasa, Tibet: Tethered balloon-based in-situ measurements and source apportionment

Liang Ran[1], Zhaoze Deng[1], Yunfei Wu[1], Jiwei Li[1], Zhixuan Bai[1], Ye Lu[1,2], Deqing Zhuoga[3], Jianchun Bian[1,2,4]

[1]Key Laboratory of Middle Atmosphere and Global Environment Observation, Institute of Atmospheric Physics, Chinese Academy of Sciences, Beijing, 100029, China

[2]College of Earth and Planetary Sciences, University of Chinese Academy of Sciences, Beijing, 100049, China

[3]Tibet Institute of Plateau Atmospheric and Environmental Science, Lhasa, 850000, China

[4]College of Atmospheric Sciences, Lanzhou University, Lanzhou, 730000, China

Correspondence to: Zhaoze Deng (dengzz@mail.iap.ac.cn) and Liang Ran (shirleyrl@mail.iap.ac.cn)

Abstract. In-situ measurements of vertically resolved particle size distributions based on a tethered balloon system were carried out for the first time in the highland city of Lhasa over the Tibetan Plateau in summer 2020, using portable optical counters for the size range of 0.124~32 μm. The vertical structure of 112 aerosol profiles was found to be largely shaped by the evolution of the planetary boundary layer (PBL), with a nearly uniform distribution of aerosols within the daytime mixing layer and a sharp decline with the height in the shallow nocturnal boundary layer. During the campaign, ~~the average~~ mass concentrations of particulate matters smaller than 2.5 μm in aerodynamic diameter ($PM_{2.5}$) within the PBL ranged from 0.5 to 12.0 μg m^{-3}, ~~was around 3~~with an average and standard deviation of 3.4±2.3 μg m^{-3}, almost four times of the amount in the free troposphere (FT), which was rarely affected by surface anthropogenic emissions. Though there was a lower level of particle mass in the residual layer (RL) than in the PBL, a similarity in particle mass size distributions (PMSDs) suggested that particles in the RL might be of the same origin as particles in the PBL. This was also ~~in consistence~~consistent with the source apportionment analysis based on the PMSDs. Three distinct modes were observed in the PMSDs for the PBL and the RL. One mode was exclusively coarse particles up to roughly 15 μm and peaked around 5 μm. More than 50% of total particle mass

was often contributed by coarse mode particles in this area, which was thought to be associated with local dust resuspension.

25 The mode peaking over 0.5~0.7 µm was representative of biomass burning on religious holidays and was found to be most pronounced on holiday mornings. The contribution from the religious burning factor rose from about 25% on non-holidays to nearly 50% on holiday mornings. The mode dominated by particles smaller than 0.3 µm was thought to be associated with combustion related emissions and/or secondary aerosol formation. In the FT coarse mode particles only accounted for less than 10% of the total mass and particles larger than 5 µm were negligible. The predominant submicron particles in the FT

30 might be related to secondary aerosol formation and the aging of existed particles. To give a full picture of aerosol physical and chemical properties and better understand the origin and impacts of aerosols in this area, intensive field campaigns involving measurements of vertically resolved aerosol chemical compositions in different seasons would be much encouraged in the future.

1 Introduction

35 Lhasa, the provincial capital of Tibet, lies almost in the heart of the sparsely populated Tibetan Plateau, which is the highest plateau in the world with an average altitude of approximately 4320 m (Zhang et al., 2021). As a result of its unique topography, the Tibetan Plateau plays a vital role in East Asian Summer Monsoon, thereby in the regional and global climate (He et al., 2019; Chiang et al., 2020). As the most urbanized and populated highland city in Tibet, Lhasa is quite suitable for exploring the impact of anthropogenic activities on atmospheric components over this remote region.

40 In the past decade, the population in Lhasa has increased from about 0.55 million in 2010 to nearly 0.87 million in 2020, according to the newly published data from the Seventh National Population Census (http://www.xizang.gov.cn/zwgk/zfsj/ndtjgb/202105/t20210520_202889.html, last access on 18 June 2021). Rapid urbanization and economic growth, also the ever thriving tourism, have given rise to a marked increase in residential, industrial

and traffic emissions. As a religious and cultural center, the widespread religious burning was also an important source for

45   various air pollutants (Cui et al., 2018b; Wei et al., 2019a). In the low oxygen-containing atmosphere (molecules per volume)

at an altitude of about 3650 m, incomplete combustion could further enhance emissions of air pollutants such as black carbon

and organic aerosols. The probable photochemically active atmosphere due to strong solar radiation at such a high altitude and

low latitude might facilitate the formation of secondary aerosols and gaseous pollutants like ozone (Lin et al., 2008), though

the extent to which secondary production is enhanced remains uncertain considering pressure-dependent reaction rate constants

50   (Atkinson, 2000). In addition, the topography of Lhasa being located in the Lhasa River Valley and surrounded by high

mountains prevents effective dilution of air pollutants. Consequently, serious air pollution comparable to the level in more

urbanized and developed cities at lower altitudes has been observed (Ran et al., 2014; Duo et al., 2018; Li et al., 2019). However,

it was demonstrated that air quality in Lhasa has been slightly improved in 2017 compared with previous years, due to the

implementation of Action Plan on Prevention and Control of Air Pollution all over China since 2013 (Yin et al., 2019).

55   Previous studies on aerosols in Lhasa were quite limited. One particular focus was the chemical composition of single particle

(Zhang et al., 2001a; Duo et al., 2015), bulk aerosol (Cong et al., 2011; Gong et al., 2011; Liu et al., 2013; Chen et al., 2018)

and size-segregated aerosols (Zhang et al., 2001b; Wan et al., 2016; Cui et al., 2018a; Wei et al., 2019a, 2019b) near the ground.

Results from these studies revealed that vehicular exhaust, religious activities which involve~~involved~~ incense burning and

biomass burning, and the suspension of mineral dust were major sources. It was also pointed out from the results of the

60   backward trajectory analysis that local emissions dominated during the monsoon season (Wei et al., 2019b). Aerosol optical

properties such as multi-wavelength aerosol absorption near the ground (Zhu et al., 2017) and aerosol optical depth (Bai et al.,

2000; Zhu et al., 2019) have also been investigated. However, the particle size distribution, as a critical microphysical property,

has rarely been studied. Using a portable optical particle counter, Cui et al. (2018b) measured particle size distributions (14

size bins) within the range of 0.14~3 μm for three weeks in summer 2016 in urban Lhasa and emphasized the significance of

religious burning to fine particles. In-situ measured vertical profiles of particle size distributions with a rather coarse size resolution were obtained from three balloon measurements in 1999 over Lhasa, but were only used to explore an enhancement in fine particle concentrations near the tropopause (Tobo et al., 2007). The vertical structure of particle size distributions and its temporal variation within the planetary boundary layer has not yet been examined. To get a better knowledge on the current status of aerosol microphysical properties in Lhasa and to advance our understanding on the influence of anthropogenic activities, in-situ measurements of vertically resolved particle size distributions with a high vertical resolution are much needed. In this study, the vertical structure and temporal variability of aerosol profiles were explored, based on in-situ measurements of particle size distributions within 1 km above the ground at a suburban site in Lhasa, using optical counters attached to a tethered balloon. Source apportionment based on measured particles size distributions was further performed to identify possible sources for aerosols in different layers.

2 Measurements

2.1 The field site

The city of Lhasa lies in an east-west oriented valley along the Lhasa River, surrounded by mountains up to an elevation of about 5500 m (Fig. 1a), as shown by SRTM data V4 from Jarvis et al. (2008). The field site is on the Najin campus of Tibet University (29.64 °N, 91.18 °E) in a suburban area of Lhasa, approximately 5 km to the east of the urban centre (Fig. 1b). As the commercial and religious centre, the urban area features crowded streets and heavy traffic, partly due to the thriving tourism and partly due to frequent religious activities. Religious burnings are constantly practiced and especially vigorous on religious ceremonies in the Potala Palace and the neighbouring famous temples, such as Jokhang Temple and Ramoche Temple, which are all located in this area and attended by many worshippers and tourists throughout the year. Comparatively, the suburb is

thinly populated with much less traffic. Thus emissions from residential, vehicular and religious sources are expected to be

85   much weaker in the surrounding area of the site than in the downtown.
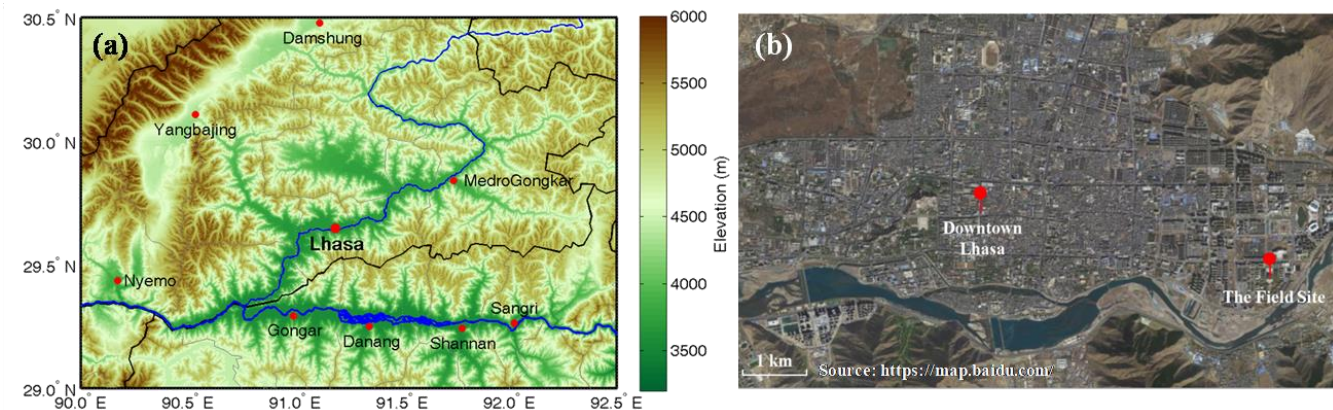
Figure 1 The topographic map of the Lhasa River Valley (a) and the city map of Lhasa (b).

2.2 Instruments and data

Measurements were conducted in an open space, being kept about 90 m away from the nearest building, in order to ensure the

90   safety of launching the tethered balloon system. The 60 m^3 helium-filled tethered balloon, with a payload capacity of roughly

10 kg at an elevation of 3650 m, was operated by an electric winch that controlled the ascent and descent rate of the fish-

shaped balloon. It was scheduled to launch the balloon to at least 800 m above the ground every 3 hours from 07:00 to 22:00

(in Beijing time) during 8-28 August 2020. The actual number of launches and the actual maximum height reached by each

flight were subject to unavailable flight permits and unfavorable weather conditions (precipitation and/or strong winds). In

95   total, 56 launches were successfully performed for the entire campaign (Fig. S1a). Most flights of the tethered balloon reached

above 600 m, with 3 launches reaching 450~500 m, 15 reaching 500~600 m, 17 reaching 600~700 m, 15 reaching 700~800

m, and 6 reaching 800~850 m. In particular, strong winds were often encountered in the late afternoon, resulting in a lack of

observations during this time period (Fig. S1b).

A light-weighted optical counter, the Portable Optical Particle Spectrometer (POPS, Handix Scientific), was attached to the tethered balloon for in-situ measurements of vertical profiles of atmospheric aerosols. Details about the principle on which the instrument operates were given in Gao et al. (2016). The POPS was calibrated by establishing a relationship between the scattering signal and the particle size before the campaign. Both polystyrene latex sphere (PSL) with known sizes and ammonium sulfate particles with sizes selected by a differential mobility analyzer were employed. Though the experimental responses of the two calibration materials generally agreed well with the simulated theoretical responses, both theoretical response curves were found highly oscillatory above the particle size of 600 nm (Gao et al., 2016). Considering that the refractive index of ammonium sulfate is closer to ambient dry aerosols than PSL (Shingler et al., 2016), a combined calibration curve from the experimental response of ammonium sulfate particles for diameters smaller than 600 nm and the smoothed theoretical response of ammonium sulfate particles for diameters larger than 600 nm was used to obtain 42 logarithmically equal size bins over the size range of 0.124~2.55 μm. ~~The POPS was calibrated before the campaign using ammonium sulfate aerosols (for diameters smaller than 1 μm) and polystyrene latex spheres (for diameters larger than 1 μm). The established relationship between the scattering signal and the particle size was used to obtain 42 logarithmically equal size bins over the size range of 0.124~2.55 μm.~~ Ambient aerosols were sufficiently dried before entering the POPS by a homemade silica gel-filled diffusion drier. Previous tests of the diffusion dryer showed that roughly 75% and 50% of the water vapor could be removed after the drying in summer and winter, respectively. As a matter of fact, the relative humidity will be further lowered inside the instrument, due to the temperature difference between the ambient condition and instrument chambers. The combined effects resulted in the relative humidity inside the POPS to be well below 20% and 30% in summer and winter, respectively. The flow rate of the instrument was regularly checked during the campaign and used for data correction. Particle number size distributions (PNSD, $n(\log D_p)=dN/d\log D_p$) were obtained with a temporal resolution of 1 s, and integrated over the whole size range to provide total number concentrations (N_a). Particle mass size distributions (PMSD,

120 $m(\log D_p) = dM/d\log D_p$) were calculated from PNSDs assuming spherical particles with a density of 1.7 g cm^{-3} (Sloane et al., 1991; Tao et al., 2014). Though the assumption of a fixed density for particles with different diameters as well as the difference between the actual density of ambient particles and the assumed one might introduce some uncertainties in the calculated PMSDs, results regarding PMSDs would qualitatively not be much affected. Mass concentrations of particulate matters smaller than 1 μm and 2.5 μm in aerodynamic diameter (PM$_1$ and PM$_{2.5}$) were obtained under the assumption that the optically

125 equivalent diameter could be considered equal to the geometric diameter and the aerodynamic diameter could be converted from the geometric diameter with a density of 1.7 g cm^{-3}. The penetration curve of SCC-2.229 cyclone at 16.7 lpm (https://bgi.mesalabs.com/wp-content/uploads/sites/35/2015/02/scc_btr-2.229.pdf, accessed on 15/03/2022) was adopted for calculating PM$_1$ mass concentrations and the penetration curve of VSCC-2.946 cyclone at 16.7 lpm (https://bgi.mesalabs.com/wp-content/uploads/sites/35/2015/02/vsccref6-2.946.pdf, accessed on 15/03/2022) was adopted for

130 calculating PM$_{2.5}$ mass concentrations. The effective diameter (D_e) was the ratio of the third-order moment to the second-order moment of particle size distributions. Similarly, the effective diameter for submicron particles ($D_{e,<1\mu m}$) and for super-micron particles ($D_{e,1\sim2.5\mu m}$) were respectively calculated for particles with the diameter smaller than 1 μm and in the range of 1~2.5 μm.

A portable aerosol spectrometer (Model 11-C, GRIMM Aerosol Technik GmbH & Co. KG), equipped with the homemade

135 silica gel-filled diffusion drier, was also employed attached to the tethered balloon for 24 launches to concurrently measure the PNSD for dry particles within the size range of 0.25~32 μm. The measuring time interval was set to be 6 s, for which 31 size channels were classified. Sizing of aerosols by the instrument was verified before the campaign for several selected diameters using polystyrene latex spheres. The PNSD measured by GRIMM 11-C was combined with the PNSD simultaneously measured by the POPS, using weighting factors in the overlapped size range, namely, from the lower size limit

140 of GRIMM 11-C ($D_{p,L}$) to the upper size limit of the POPS ($D_{p,U}$). The weighting factors for GRIMM 11-C were derived as

$w_{\text{11-C}}(\log D_{\text{p}})=(\log D_{\text{p}}-\log D_{\text{p,L}})/(\log D_{\text{p,U}}-\log D_{\text{p,L}})$, while for the POPS they were defined as $w_{\text{POPS}}(\log D_{\text{p}})=(\log D_{\text{p,U}}-\log D_{\text{p}})/(\log D_{\text{p,U}}-\log D_{\text{p,L}})$. An example of combining the PNSD from POPS and GRIMM 11-C and the PMSD from POPS and GRIMM 11-C using the weighting factors for each instrument was illustrated in Fig. S2.

Vertical profiles of meteorological parameters, including pressure (MS5540B, Intersema Sensoric SA), temperature (T) and relative humidity (RH) (SHT7x, Sensirion), as well as winds (homemade sensor based on a slotted optical switch (OPB610, TT Electronics) and an electronic compass module (ZCC211N, Shanghai Zhichuan Electronic Tech Co., Ltd)) were measured for each flight with a temporal resolution of 1 s. Potential temperature (θ) and specific humidity (q), two conservative quantities, were calculated following the equations in Ran et al. (2016). Besides, surface meteorological parameters in August were available from an Automatic Weather Station roughly 4.5 km to the northwest of the site in urban Lhasa and were averaged into hourly data, except that winds were recorded as 2-min averages at the beginning of each hour.

Profiles of aerosol and meteorological parameters were all processed into 10 m-averaged data for the subsequent analysis. A mixed layer (ML) for daytime profiles or a nocturnal boundary layer (NBL) for nighttime profiles, mentioned altogether as the planetary boundary layer (PBL) in what follows, could be identified for 72 profiles in the dataset of totally 112 profiles. For the remaining 40 profiles, the flight path was entirely within the daytime ML. The height of the PBL, denoted as H_{m} hereafter, was estimated from profiles of aerosols and meteorological parameters based on the gradient method (Seibert et al., 2000; Kim et al., 2007; Ferrero et al., 2010; Ran et al., 2016). For profiles with the top of the ML above the flight limit, H_{m} was taken as the maximum height reached by the tethered balloon for further statistical analysis. The normalized height (H_{Nor}) was then calculated as height/H_{m}-1 (Ferrero et al., 2014). For several profiles, the free troposphere (FT) that was identified as the layer above the PBL without the presence of elevated aerosol layers or the residue from aerosols in the daytime after the collapse of the ML, as well as the residual layer (RL) could also be identified. In addition, the time mentioned anywhere in this study was Beijing time, which was around two hours earlier than local solar time.

2.3 Positive Matrix Factorization (PMF)

A bilinear factor-based receptor model, Positive Matrix Factorization (PMF), was used for source apportionment of particle mass in this study based upon observed PMSDs (Paatero and Tapper, 1994; Paatero, 1997). By minimizing an objective function Q, a key parameter to review the distribution of the components and to estimate the stability of the solution (Brown et al., 2015), the measured matrix was decomposed into factor profiles (F) and factor contributions (G) with non-negativity constraints. The input matrix, comprising PMSDs (22 size bins within 0.124~15 μm) averaged for the ML, the RL and the FT, and the lower 10-m averaged PMSDs in the NBL, was used in 20 random PMF runs (using EPA PMF5.0 software) for 2 to 5 factors. In total, there were 48 PMSDs for the ML, 23 PMSDs for the RL and 10 PMSDs for the FT. The components in the PMF runs were separated to keep one signal rather significant from those dominated by noise on account of a criterion of the signal-to-noise ratio (S/N) (Amato et al., 2009). The components with the S/N less than 2 were removed from further analysis, while components with the S/N above 2 were set as "strong" ~~species~~ aerosol types (Paatero and Hopke, 2003). The stability of converged Q values was found for all runs. By estimating diagnostic errors, the 3-factor result was found to be the optimal solution, with all factors mapped in 100% of the Bootstrap run, no swap of Displacement and no swapping case of Bootstrap-Displacement. The results of the scaled residuals for the 3-factor outcome were within an acceptable range of (–3, 3) (Juntto and Paatero, 1994). The measured and PMF-simulated total particle mass concentrations were significantly correlated (R^2=0.89~~0.90~~).

3 Results and discussion

3.1 An overview of meteorological conditions

Under the impact of the Asian Summer Monsoon, Lhasa normally experienced a rainy season from May to September (Ding, 2007; Ran et al., 2014). However, in August 2020 when the campaign took place, two periods with distinctly different

conditions of water vapor were found, as could be clearly seen from q near the ground measured in urban Lhasa (Fig. 2a). The sharp reduction in q during the daytime of 17 August was an indicator of changing from a humid Period I (~~averagely~~average 11.1 g kg^{-1}) to a relatively dry Period II (~~averagely~~ average 8.1 g kg^{-1}). Period I was also characterized as rainy with the

185   precipitation amounting to 78.5 mm and quite cloudy for most of the time, while there was plentiful sunshine and almost no precipitation during Period II (Fig. 2a). Rainfall mostly occurred in the evening and at night (20:00-08:00), accounting for 84% of the total amount in that month. The two periods differed not much in T, which ranged from 8.8~ to 26.8 °C in Period I and from 8.6~25.0 °C in Period II with an average of about 17.0 °C for both periods. In contrast, RH averaged nearly 62% in Period I, but only 45% in Period II (Fig. 2b), corresponding well to the difference in q. The temperature shared a similar pattern on

190   each day, except that the maximum value in the daytime apparently lowered on days with an overcast sky. Unlike the diurnal variation of T being a peak in the late afternoon (around 18:00) and a valley in the early morning (around 09:00) without much differences between the two periods, average RH reached a maximum in the early morning of about 79% ±11% for period I and 64% ±6% for Period II, as well as a minimum in the late afternoon of about 43% ±11% for period I and 28% ±11% for Period II. Surface winds were largely under 4m s^{-1} and dominated by easterly and westerly winds (Fig. 2c).

195   Vertical profiles of meteorological parameters observed at the site were categorized into five time periods of the day as give in Table S1, and were presented along H_{Nor}, if either a ML or a NBL could be identified, for a straightforward comparison between the two periods (Fig. S3~2~). The amount of moisture was obviously higher in Period I than in Period II for all time periods, being consistent with what had been revealed from continuous surface measurements. The conservative quantities, θ and q, were generally uniform in the ML for daytime profiles, whereas T decreased and RH increased with increasing height,

200   respectively. For profiles collected during 07:00-08:00 and 20:00-23:00, air temperature inversions in the NBL were recognized for several cases. On average~~Averagely~~, there was a slight increase in θ and decrease in q along with increasing height. Accordingly, wind speed apparently increased with increasing height. A further examination on the probability

distributions of wind speed and wind direction indicated that winds were mainly below 4 m s^{-1} both within and above the PBL throughout the campaign, also being dominated by easterly and westerly winds as near the ground (Fig. S4̶3). Stronger easterly

205 winds exceeding 4 m s^{-1} occurred above the PBL, even up to nearly 7 m s^{-1} in Period II. It should be kept in mind that data points available for calculating time-period averages at some heights above the PBL, corresponding to H_{Nor} larger than 0, might make up only a part of the total number and might thus introduce misleading details. Caution should thereby be taken about statistically drawing conclusions from the characteristics of height-normalized profiles across the PBL and at different heights above the top of the PBL. ~~The l~~Last but not ~~the~~ least, the analysis regarding meteorological parameters, especially winds, was

210 somewhat limited to measurements under a relatively mild condition when the tethered balloon were able to be launched.
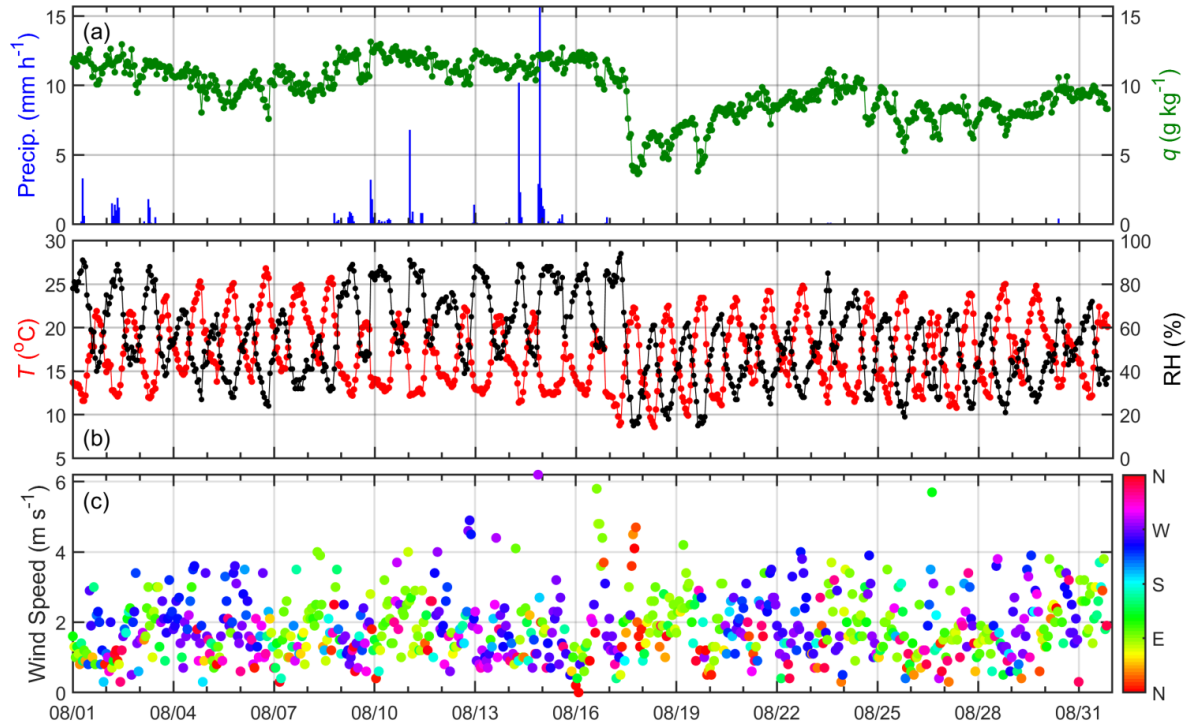
Figure 2 The time series of (a) precipitation in blue and specific humidity (q) in green, (b) temperature (T) in red and relative humidity (RH) in black, (c) wind speed and wind direction (in colours), based on hourly data in August from an Automatic Weather Station in urban Lhasa.

3.2 The vertical structure and temporal variability of aerosol profiles

3.2.1 Vertical distributions and diurnal variations of aerosol properties

The evolution of the PBL was an important influencing factor in shaping the vertical structure of atmospheric aerosols, as has been ~~being already~~ pointed out by some previous studies (Ferrero et al., 2010; Rant et al., 2016; Zhang et al., 2017). During the campaign, heights of the shallow NBL were largely below 200 m around sunrise/sunset and at night (Fig. S54). In Period I, H_m could be determined for most profiles before midday around 14:00, possibly resulting from the development of the ML being suppressed under usually cloudy conditions. In the afternoon, the ML often developed higher than the maximum height reached by the tethered balloon. Unfortunately, intensive observations covering a day from the early morning until the night were unavailable, either because of unobtainable aviation permission or bad weather. Nevertheless, relatively frequent measurements on 12 August (marked by black cross in Fig. S54) revealed, in a more realistic way as compared with what the overall picture could tell, the gradual increase of H_m in the overcast morning, from below 100 m before sunrise to about 700 m towards noon. The depth of the ML on that day was expected to be far above the flight limit of 500 m in the afternoon, since it turned to be quite sunny and cloudless overhead after midday. As for Period II, the ML should have developed very quickly after sunrise on those sunny days, thus H_m were often already high above the flight limit when aviation permissions were granted in the late morning and the afternoon.

Normalized by H_m, average vertical profiles of aerosol properties in five time periods of the day were illustrated in Fig. 3, exhibiting a similarity between Period I and II. Profiles of N_a and particle mass concentrations around sunrise (07:00-08:00) and since evening (20:00-23:00) resembled an exponential decay in the stable NBL, which favored the accumulation of air pollutants near the ground. In the daytime, profiles were characterized by a nearly uniform distribution of aerosols within the ML, except for profiles collected during 08:00-12:00 in Period II with the characteristics of nighttime profiles. This misleading feature was attributed largely to profiles on religious holidays that were frequently encountered in Period II with the impact of

strong emissions from religious burning in the morning, which will be discussed in detail in Sect. 3.3. With the evolution of

the ML, stronger dilution effects led to a decline in surface N_a and particle mass concentrations in the daytime, compared to

that in the early morning and at night. However, surface N_a and particle mass concentrations were found to be the highest

during 08:00-12:00 in both periods. The reasons for this phenomenon might be enhanced emissions from more anthropogenic

240   activities after sunrise but still weak dispersion inside a ML, where vertical convection had not been fully developed. Above

the PBL, the number of data points used for averaging varied with H_{Nor}, depending on H_m and the maximum height of each

flight. To avoid being misled by insufficient data, averaged data were only adopted at heights where the data availability

exceeded 75%. An evident reduction in N_a and particle mass concentrations above the PBL was observed by comparison with

that within the PBL. For both periods, ratios of PM$_1$ to PM$_{2.5}$ mass concentrations (PM$_1$/PM$_{2.5}$) were relatively uniform within

245   the PBL even for NBL-type profiles, despite distinctly different aerosol amount along the normalized height in the NBL. The

daytime PM$_1$/PM$_{2.5}$ ratios were relatively larger than ratios in the early morning and at night. Accordingly, D_e was found to be

relatively smaller during the day.

Table 1 listed particle parameters in the PBL, the RL and the FT. For the PBL category, averages within the ML and 10-m

averages near the ground for the NBL were adopted. Inside the well mixed layer, the surface level and the ML-averaged level

250   were close to each other. Averaged N_a within the PBL was about 338±162 cm^{-3} in Period I and 409±201 cm^{-3} in Period II. The

mean PM$_{2.5}$ mass concentration within the PBL was ~~2.7±1.7~~ 2.9±1.8 μg m^{-3} in Period I, with a fraction of PM$_1$ in PM$_{2.5}$ to be

about ~~81±6~~ 76±6%. In Period II, PM$_{2.5}$ mass concentrations within the PBL averaged ~~3.6±2.4~~ 3.9±2.6 μg m^{-3}, with PM$_1$

accounting for approximately ~~73±9~~ 68±10%. The lower level of aerosols in Period I might be ascribed to frequent rainfalls

and associated efficient removal processes. Submicron particles took up a smaller proportion in PM$_{2.5}$ during Period II, together

255   with a larger average D_e of ~~0.35~~ 0.37 and a larger average $D_{e,1\sim2.5\mu m}$ of ~~1.76~~ 1.67, indicating more large particles in Period II

than in Period I. Though average $D_{e,<1\mu m}$ in the two periods was comparable with each other, a wider range was found in Period

II, showing the large variability in particle size distributions among profiles collected at different time.
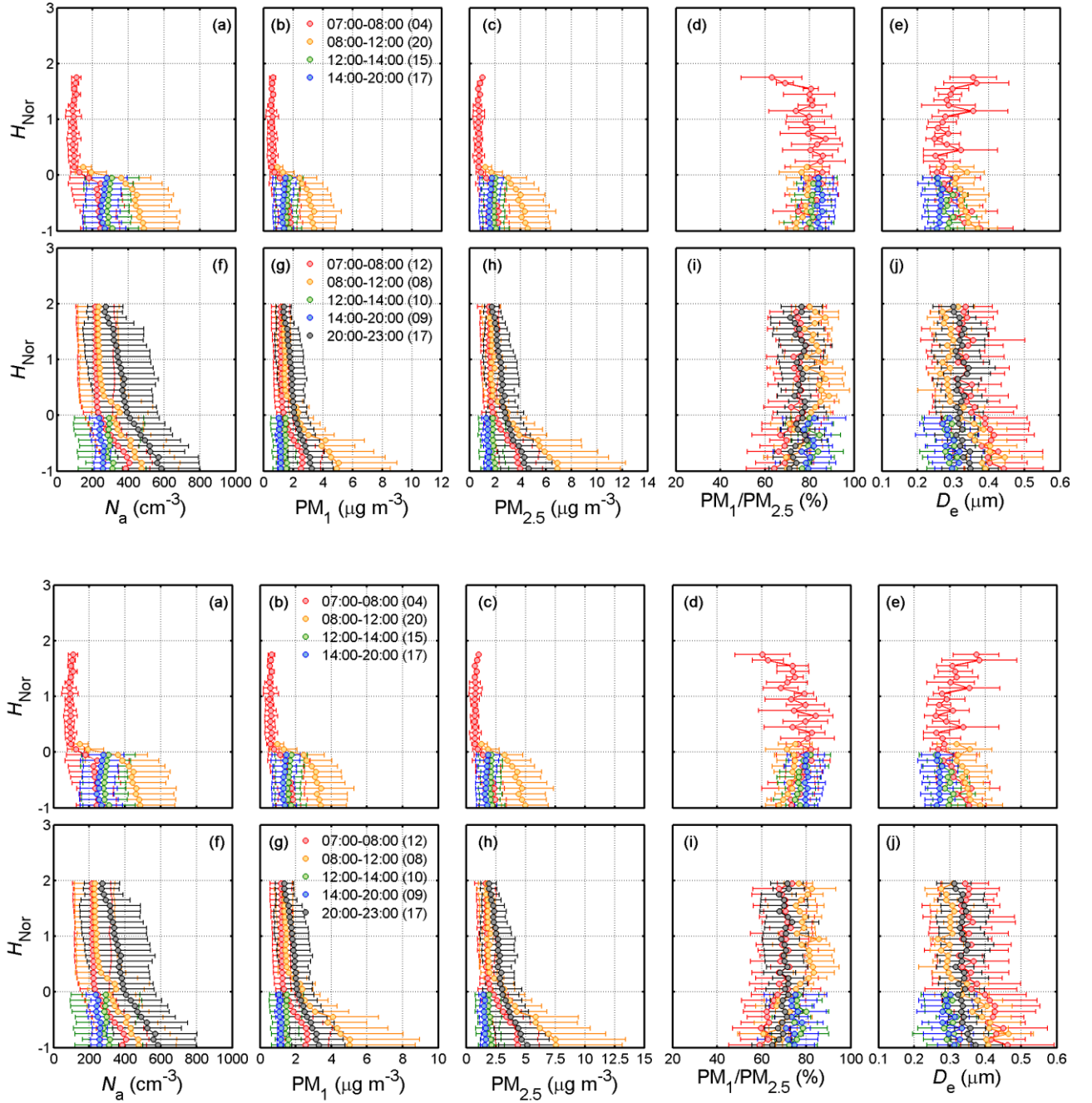
Figure 3 Average vertical profiles of (a) particle number concentration (N_a), (b) PM$_1$ mass concentration, (c) PM$_{2.5}$ mass concentration, (d) the ratio of PM$_1$ to PM$_{2.5}$ mass concentration, and (e) the effective diameter (D_e) over the whole size range of the POPS, along the normalized height (H_{Nor}) during Period I. Profiles for different time periods are shown in different colours, with dots representing average values and error bars representing standard deviations at each of the H_{Nor}. The number of data points used for averaging at each H_{Nor} was more than about 75% of the number of profiles during each time period, as given in parentheses.

265 **Average vertical profiles measured during Period II are displayed in the same way in (f)-(j).**

It was found that ~~average~~ PM$_{2.5}$ mass concentrations within the PBL ranged from 0.5 to 12.0 µg m^{-3} with an average of 3.4 µg m^{-3} and a standard deviation of 2.3 µg m^{-3} during this campaign. ~~(3.1±2.1 µg m^{-3})~~ PM$_{2.5}$ mass concentrations in this study were far below what had been observed near the ground in August 2016 in urban Lhasa, where the high levels often exceeded 20 µg m^{-3} and were sometimes up to more than 40 µg m^{-3}, with the overall average to be 11±2.2 µg m^{-3} over the size range of

270 0.14~3 µm (Cui et al., 2018b). The significant difference of particle mass concentrations between the previous and the current study might reflect different emission strengths surrounding the two sites. Being located in the downtown area and adjacent to several temples, the observational site in the previous study was greatly affected by various strong local emissions, such as traffic, residential and religious activities-related emissions, while the suburban site in this study was under the influence of much weaker nearby emissions and more likely to represent an average condition over this area. Furthermore, the continuous

275 monitoring of PM$_{2.5}$ mass concentrations from 2013 to 2017 at 6 sites across the city of Lhasa revealed a slight decrease in 2017 (Yin et al., 2019). This was demonstrated to be partly attributed to measures taken to prevent and control air pollution in Lhasa since 2013. Actually, the location of the site in this study was on the same campus of Tibet University as one site (LHASA-XZ) in Yin et al. (2019). Considering that monthly mean PM$_{2.5}$ mass concentration of all 6 sites for August was reported as about 15 µg m^{-3} and the LHASA-XZ site was not the cleanest one among the others, it might suggest an apparent

280 reduction in PM$_{2.5}$ mass concentrations with the continuing implementation of air quality policies.

Table 1 Particle parameters within the PBL, in the RL and in the FT for Period I and II, given as average value ± standard deviation and the range in parentheses. The number of profiles for each category is also given in parentheses in the second row.

	PBL		RL		FT	
	Period I (56)	Period II (56)	Period I (0)	Period II (29)	Period I (14)	Period II (10)
N_a (cm^{-3})	338±162 (77~812)	409±201 (95~~~1052~~1051)	/	299±101 (123~~~573~~575)	89±37 (47~156)	81±23 (44~~~111~~112)
PM$_1$ (μg m^{-3})	2.1±1.3 (0.4~5.5)	2.6±1.7 (0.5~7.8)	/	1.6±0.6 (0.6~3.1)	0.5±0.2 (0.3~1.1)	0.5±0.3 (0.2~0.9)
PM$_{2.5}$ (μg m^{-3})	~~2.7±1.7~~2.9±1.8 (0.5~~~8.6~~7.8)	~~3.6±2.4~~3.9±2.6 (~~0.6~10.9~~0.7~12.0)	/	~~2.0±0.7~~2.2±0.8 (0.9~~~4.2~~4.0)	0.7±0.3 (~~0.3~~0.4~1.3)	~~0.7~~0.8±0.4 (0.3~~~1.3~~1.1)
PM$_1$/PM$_{2.5}$ (%)	~~81±6~~76±6 (~~62~90~~59~88)	~~73±9~~68±10 (~~48~93~~44~92)	/	~~78±5~~72±5 (~~69~86~~62~83)	~~79±5~~75±6 (~~71~87~~65~82)	~~76±9~~71±10 (~~63~89~~57~86)
D_e (μm)	~~0.30~~0.31±0.06 (~~0.20~~0.21~0.47)	~~0.35±0.09~~0.37±0.10 (0.21~~~0.65~~0.61)	/	~~0.31~~0.32±0.03 (0.26~~~0.39~~0.37)	~~0.29~~0.30±0.04 (~~0.24~0.36~~0.25~0.38)	~~0.34±0.07~~0.35±0.08 (0.24~~~0.48~~0.46)
$D_{e,<1\mu m}$ (μm)	~~0.23~~0.22±0.03 (0.19~~~0.30~~0.31)	0.23±0.04 (0.18~0.35)	/	~~0.22~~0.21±0.01 (~~0.20~~0.19~0.24)	0.22±0.01 (~~0.20~~0.19~0.24)	0.23±0.03 (0.18~~~0.26~~0.27)
$D_{e,1\sim2.5\mu m}$ (μm)	~~1.71±0.15~~1.61±0.09 (1.34~~~1.92~~2.46)	~~1.76±0.13~~1.67±0.11 (~~1.26~2.00~~1.35~1.90)	/	~~1.72±0.08~~1.65±0.07 (~~1.56~1.87~~1.50~1.74)	~~1.58±0.11~~1.51±0.09 (~~1.40~1.76~~1.36~1.61)	~~1.62±0.18~~1.56±0.13 (~~1.32~1.78~~1.36~1.70)

Profiles in Period II were mainly collected in the early morning and at night, when elevated aerosol layers were often encountered, though it was hard to tell whether those were only residual layers that could easily form above the NBL after sunset and remain until the PBL had evolved to ~~an enough~~sufficient height ~~in~~ the next day, or if there could also be contributions from transported plumes. Here, we generally denoted such elevated layers as residual layers (RL). In total, the RL was identified for 29 profiles in Period II, whereas none was identified in Period I. A layer above the PBL and beneath the FT was observed for four profiles collected in the morning in Period I, with N_a to be a little higher than that in the FT but still very low (~100 cm^{-3}). Since it was insufficient to decide whether the layer was the RL or still a part of the FT, also it would be misleading if they were used to represent the average condition of the RL during Period I, they were identified as neither the RL nor the FT. ~~No RL were observed during Period I.~~ In Period II, the average particle number and mass concentrations in the RL were respectively around 75% and 55% of that within the PBL. In the FT, average particle number and mass

concentrations in the two periods were generally comparable with each other, and were ~~almost~~ generally less than 25% of the amount within the PBL. In general, fractions of PM_1 in $PM_{2.5}$ within the PBL were close to those in the RL and the FT for each

295 period.

Undoubtedly, air quality over the Tibetan Plateau has been increasingly influenced by anthropogenic activities and emissions during the processes of urbanization and economic growth in the past several decades, especially in relatively thickly populated cities like Lhasa. However, the level of N_a over Lhasa was still much lower than what has been observed in more populated and developed regions. Aircraft measurements of particles with the diameter ranging from 0.1 μm to 3.0 μm using a passive

300 cavity aerosol spectrometer probe (PCASP) over the Loess Plateau, which is adjacent to the Tibetan Plateau, revealed that N_a in the PBL often exceeded 1000 cm^{-3} and N_a above the PBL reached well above 200 cm^{-3} for most flights during the summer campaign 2020 (Cai et al., 2021). Influenced more by anthropogenic emissions, N_a over the Loess Plateau were more than 3 times of those obtained within and above the PBL over Lhasa. Though a slightly larger average D_e of around 0.4 μm was observed over the Loess Plateau, no apparent dependence of D_e on altitude was found in both locations. Aircraft measurements

305 that also employed PCASP in non-winter seasons during 2005 and 2006 over Beijing in the polluted North China Plain showed that the surface level of N_a ranged from 1000 cm^{-3} (10th percentile) to 10000 cm^{-3} (90th percentile) and averaged as high as 6600 cm^{-3}, more than 10 times of that over Lhasa (Liu et al., 2009). Aerosol profiles measured by a tethered balloon-born OPC over Milan in Italy, which is also located in a river valley (the Po Valley) but in a region much more industrialized and populated than the Lhasa River Valley, exhibited an average N_a of 35 ± 2 cm^{-3} in the diameter range of 0.3~20 μm above the

310 PBL in summer (Ferrero et al., 2010). Given the same size range, a lower level of particle number concentrations was found in the FT over Lhasa, with the average N_a to be 12 ± 8 cm^{-3}.

3.2.2 Vertically resolved particle mass size distributions

Particle mass size distributions (PMSD) measured by the POPS were categorized into two periods and averaged for three layers (Fig. 4). In general, size-resolved particle mass concentrations were the highest at all diameters within the PBL, while
315 much lower in the FT. Nevertheless, a similarity was found among all PMSDs. Plainly, a distinct mode below ~~around 0.23~~0.3 μm existed for all layers during both periods, though its relative strength to the rest part of the PMSD considerably differed among different layers and periods. For this mode, more particles were observed towards the lower end of the size range in Period II, possibly implying stronger secondary formation of fine particles favored by the fine weather during that period. It was noteworthy that the small peak around 0.23 μm might be resulted from uncertainties in the measurement or calibration.
320 Thus, caution should be taken when drawing specific conclusions. Particles larger than 1 μm apparently increased with the diameter for all PMSDs, suggesting another mode in coarse particles. The normalized averages of PMSDs that were merged from the POPS and GRIMM 11-C measurements over the size range of 0.124~32 μm, which were only available for 48 profiles in Period II, did exhibit a mode peaking around 2.5 μm in the FT and around 5 μm in the other two layers (Fig. S6~~5~~). Particles as large as roughly 15 μm were observed within the PBL and in the RL. In contrast, particles with the diameter larger than 5
325 μm accounted only for a negligible part of the PMSD in the FT. It was also noted, from both the average PMSD (Fig. 4) and the normalized average PMSD (Fig. S6~~5~~), that there was a third mode ranging over 0.5~0.7 μm within the PBL and in the RL, though relatively less pronounced for the later one, whereas no such an apparent mode was observed in the FT. These features revealed that under most circumstances particles in the RL were of the same origin as particles in the PBL, whereas particles in the FT should be rarely affected by local anthropogenic emissions near the ground.

330
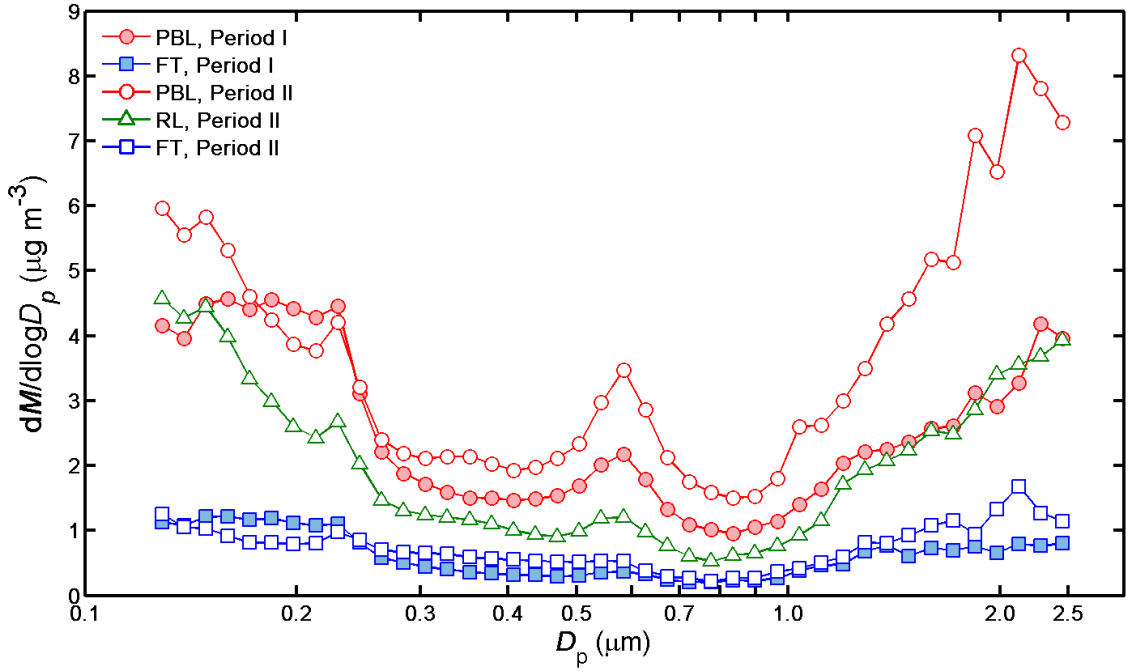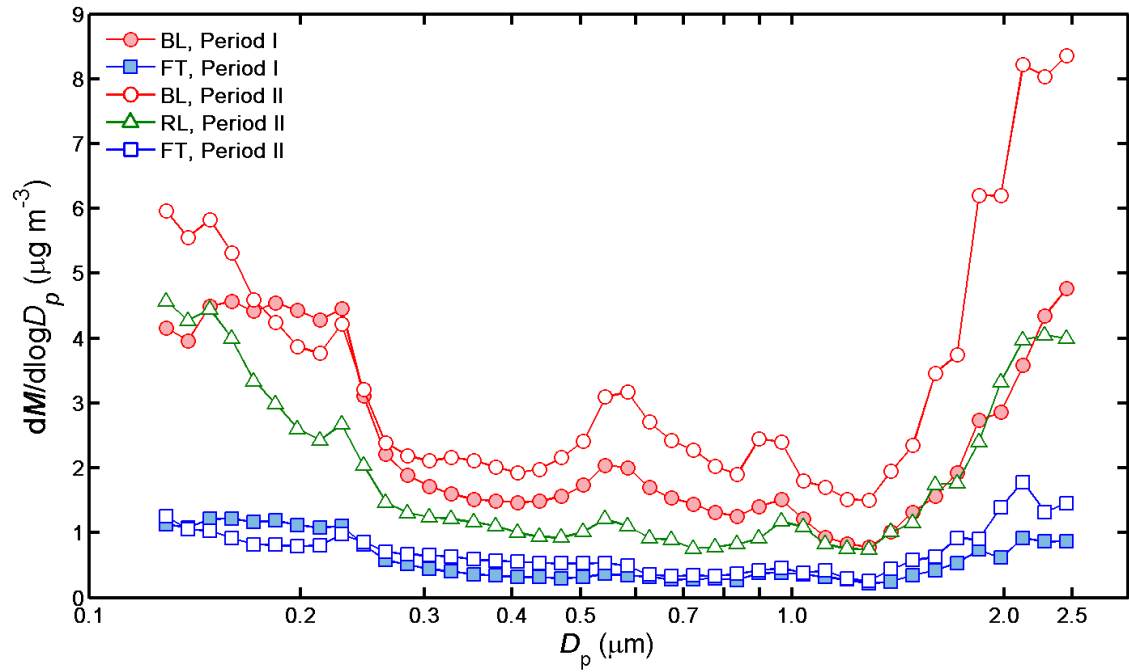
Figure 4 Average particle mass size distributions (dM/dlogD_p) for different layers during the two periods as indicated by different markers.

The vertical distribution of PMSDs within the size range of 0.124~32 μm for each profile in Period II was explored in more

335   detail. It was noteworthy that the mode over 0.5~0.7 μm was found to be more distinct on the mornings of religious holidays

compared with that at other times. In order to conveniently make comparisons among different cases, the dataset was grouped

into subsets of data collected on non-holidays and holidays. In total, there were 22 aerosol profiles collected on non-holidays

and 26 on the four religious holidays (19, 20, 26, 28 August). The subset of data from holidays was further divided into five

cases, four of which respectively comprised measurements on the morning of each religious holiday. One case, consisting of

340   data collected on holidays except in the morning, was denoted as holidays* to distinguish from the category named holidays

that covered all profiles measured on religious holidays. The average profile of $D_{e,<1μm}$ on non-holidays and holidays* were

found to be close to each other, with an average of roughly 0.21 ±0.006~~0.01~~ μm and ~~0.23 ±0.02~~0.20 ±0.005 μm through the

vertical direction, respectively (Fig. 5a). However, the average vertical distribution of $D_{e,<1μm}$ on the morning of each religious

holiday, as separately displayed in different colors, was significantly different from the categories of non-holidays and

345   holidays*. In the PBL, a remarkably larger $D_{e,<1μm}$ was observed in the morning on all religious holidays than that on both non-

holidays and holidays*. The largest $D_{e,<1μm}$ was nearly 0.35 μm on 19 August, the Shakyamuni Buddha Day and also the

beginning of Sho Dun Festival, one of the most ceremonious traditional festival in Tibet. This could plausibly explain the

aforementioned larger range of $D_{e,<1μm}$ averaged within the PBL in period II than in Period I, since emissions from religious

activities on religious holidays enlarged the effective diameter and only one religious holiday (8 August) was encountered in

350   Period I. Above the PBL, $D_{e,<1μm}$ for the four holiday morning cases generally fell in the range of $D_{e,<1μm}$ on non-holidays and

holidays, except that $D_{e,<1μm}$ on the morning of 19 August was apparently larger than others. As for coarse particles in the size

range of 1~10 μm, no obvious difference was observed between non-holidays and holidays (Fig. 5b).
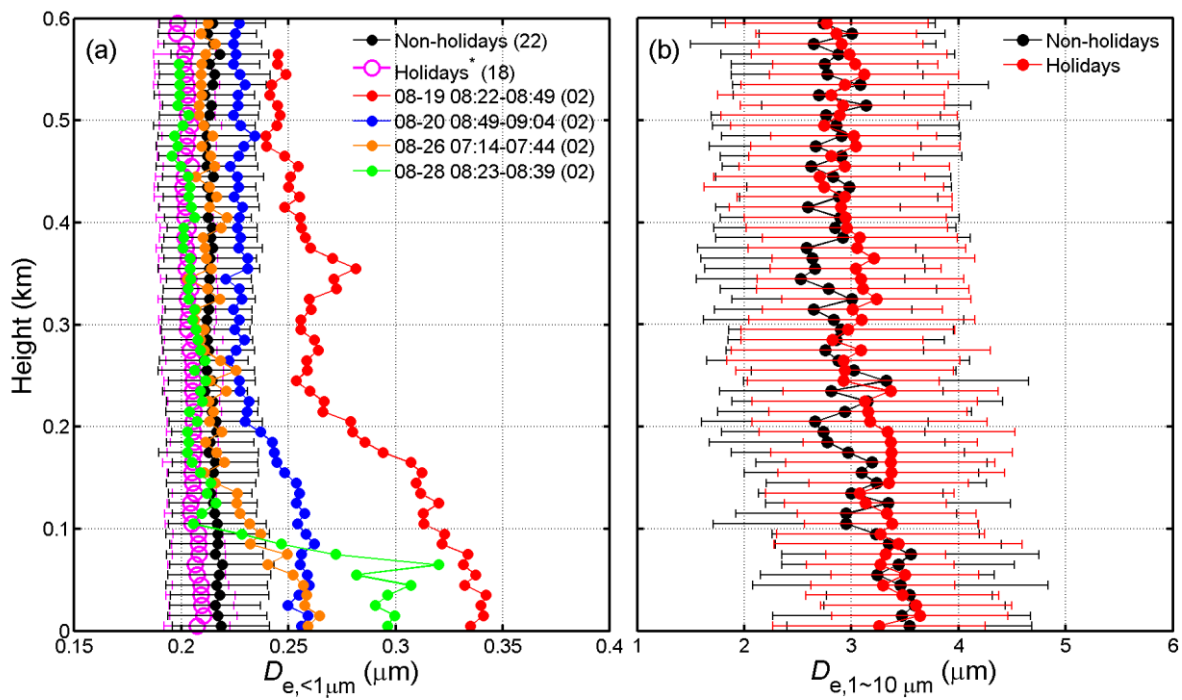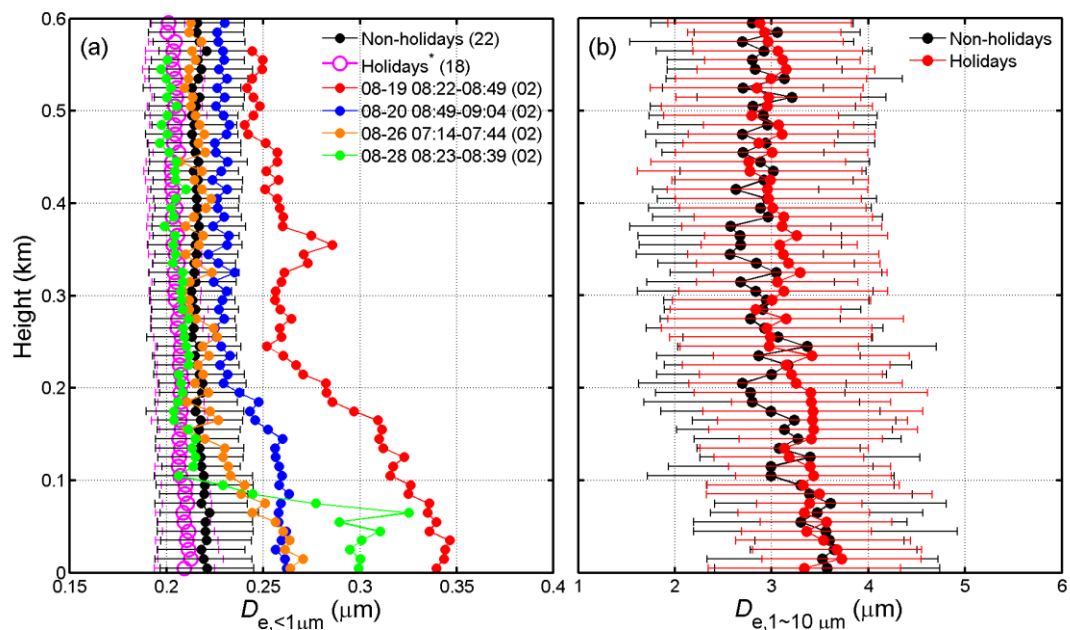
355 **Figure 5 (a) Average vertical profiles of $D_{e,<1\mu m}$ for different cases: solid black dots for non-holidays, magenta circles for religious holidays but excluding samples in the mornings, various colored solid dots for religious holiday mornings. (b) Average vertical profiles of $D_{e,1\sim10\mu m}$ for non-holidays (black dots) and holidays (red dots). The number of profiles collected during the period of each case was given in the parentheses.**

A further examination was taken on average PMSDs within 50 m above the ground for each category, considering that in the

360 NBL or in an early morning ML measurements near the ground would better help elucidate the impact religious activities

brought to PMSDs. A marked mode peaking around 0.6 μm and amounting to about 18 μg m^{-3} was observed in the PMSDs on

19 and 28 August (Fig. 6). Though much lower around 5 μg m^{-3} on 20 and 26, the peak of this mode was still almost double

of that on non-holidays and holidays*. The existence of the accumulation mode over 0.5~0.7 μm on religious holidays was

consistent with the findings from surface aerosol measurements in August 2016, and was demonstrated to be characteristic of

365 emissions from incense burning and biomass burning for religious ceremonies (Cui et al., 2018b and references therein). As a

widespread religious custom, incense burning was commonly performed in the daily life of local people, not only in temples

but also at home. The burning of several types of wood branches and herbs as well as butter lamps in temples was also

traditional religious activities. The PMSDs clearly showed that these emissions were largely enhanced on holidays especially

in the mornings and formed a much strengthened accumulation mode.

370
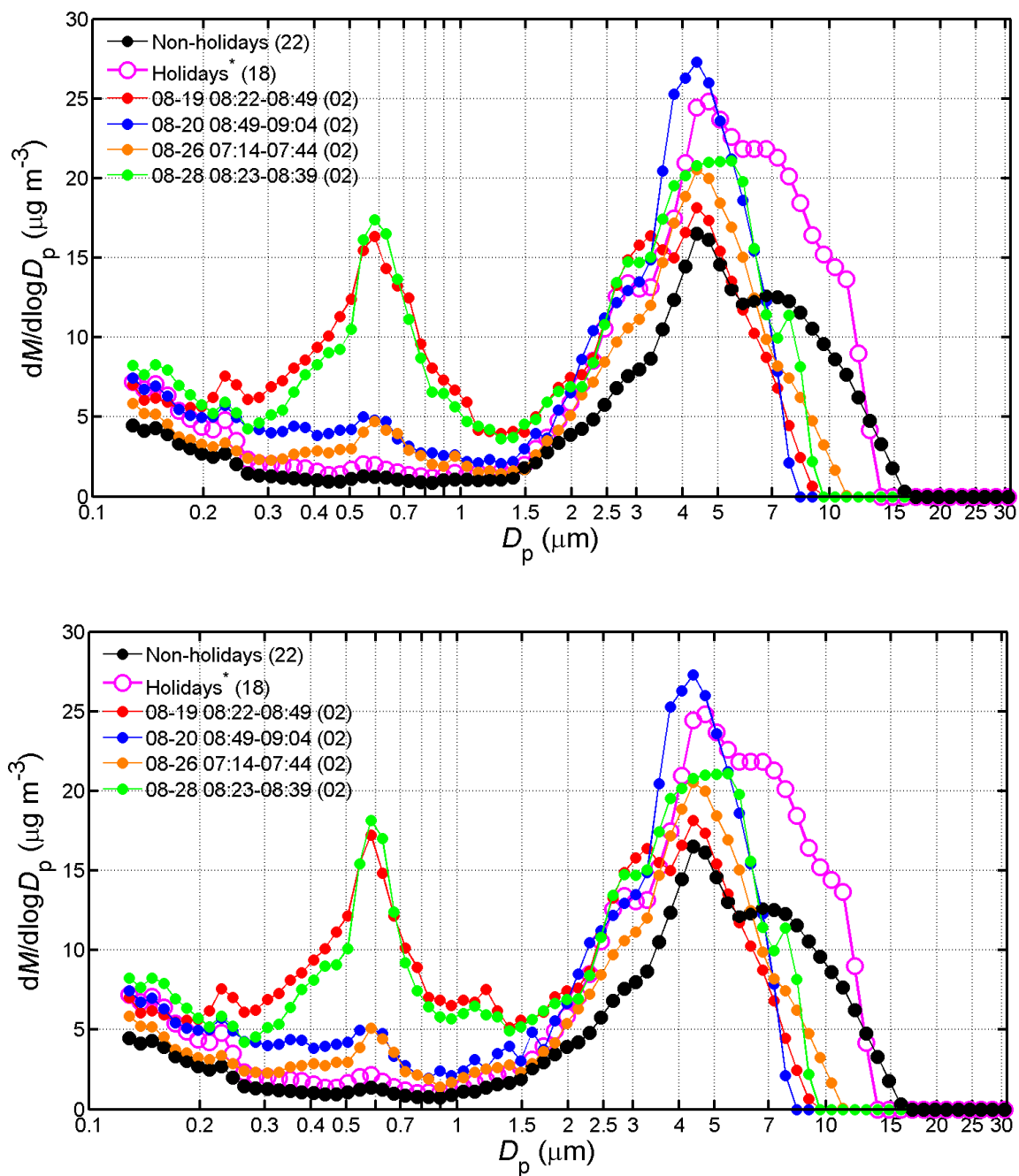
Figure 6 Average PMSDs within 50 m above the ground for different cases, with the same markers and texts as in Fig. 5.

3.3 Potential sources of particles in different layers

Three source factors were identified from the PMF analysis of the PMSDs combined from the POPS and GRIMM 11-C

375 measurements in Period II (Fig. 7a). The first factor (factor 1) revealed a potential source that predominantly contributed to

particles smaller than 0.3 μm, probably being associated with local emissions from fossil fuel combustions and/or secondary

aerosol formation. The second factor (factor 2) showed a broad peak over about 0.3~0.7 μm, with also a considerable

contribution from particles with the diameter extending from 0.7 μm to around 2.5 μm. Considering the apparent enhancement

of particle mass in the size range of 0.5~0.7 μm on religious holiday mornings, factor 2 was taken to be mainly representative

380 of aerosols released from religious activities such as burning incense, cypress branches, herbs, and butter lamp (Cui et al.,

2018b and references therein). The third factor (factor 3) was almost exclusively composed of particles in the coarse mode (>

1 μm). This factor might be attributed to suspended dust particles from unpaved roads, construction sites, and the surrounding

mountains. Indoor particles previously collected at a temple in Lhasa exhibited a bimodal particle mass distribution, with one

peak around 0.4~0.7 μm and one peak in the coarse mode around 5 μm (Cui et al., 2018a). It was speculated that factor 3 might

385 also involve a certain contribution from religious burning and/or residential biomass burning. However, concentrations

contributed by factor 3 did not increase as expected with the rising concentrations contributed by factor 2 on holiday mornings,

when assuming that coarse mode particles observed at the site were partly generated from religious activities (Fig. S76). Also

residential burning of biomass including cow dung and plants, as an important source in the past for energy, was negligible

nowadays and mostly replaced by a mixture of fossil fuel and renewable energy sources such as solar, wind, geothermal and

390 hydroelectric power.
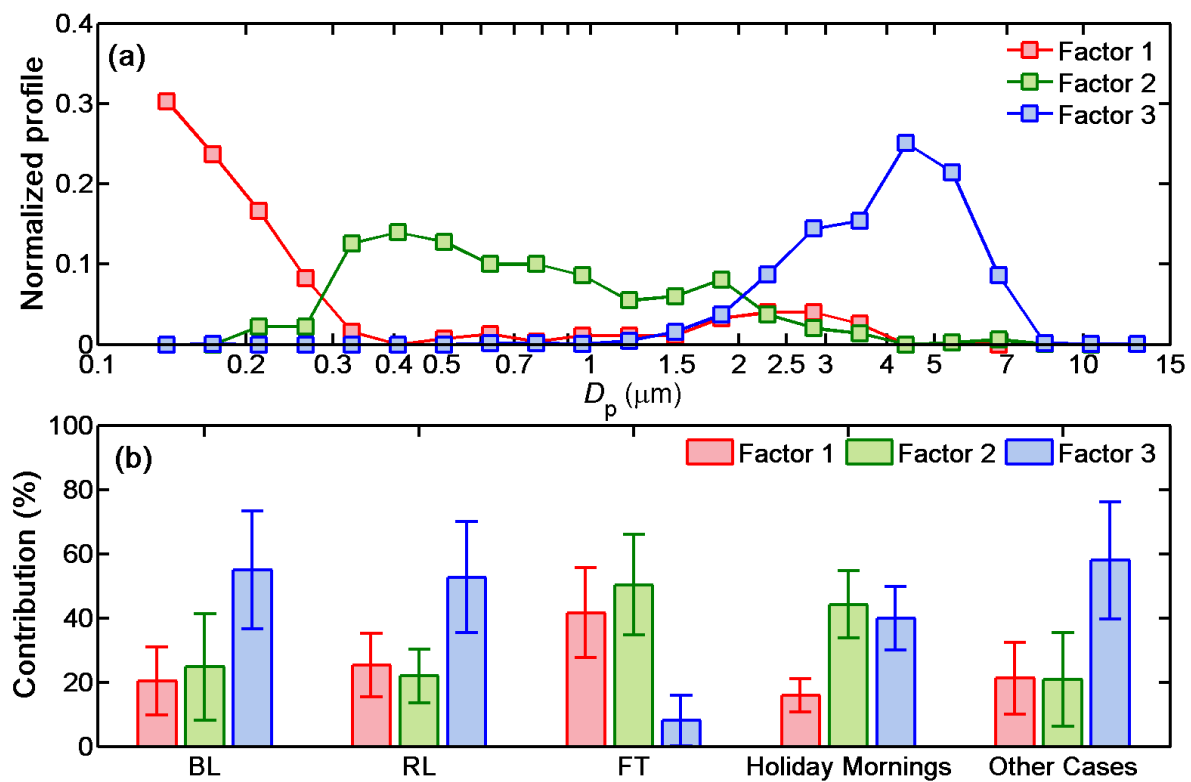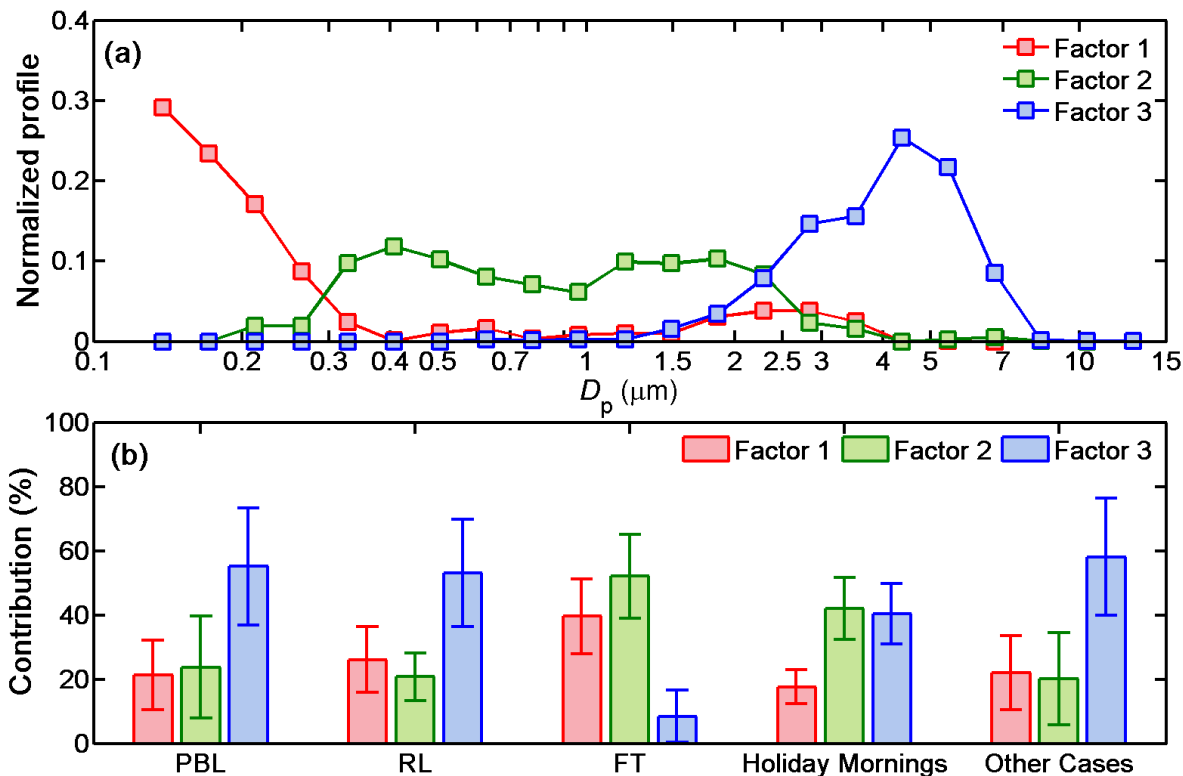
Figure 7 (a) Normalized factor profiles and (b) averaged contributions of each factor to total particle mass concentrations in the PBL, the RL, and the FT in Period II, also for averages in the PBL on holiday mornings and other cases, namely, non-holidays and holiday*, with the error bar indicating the standard deviation.

On average, particles in the PBL and the RL shared a similar makeup of potential sources (Fig. 7b), suggesting that particles in the two layers were probably of the same origin. The contribution by suspended dust particles took up a portion of more than 50%, while the contribution by religious burning was comparable with the contribution by combustion related or secondary formation source with a fraction of roughly 20%~25%. Particularly, the results for the PBL were separated into one part on holiday mornings and the other under other conditions, namely, non-holidays and holidays* as defined above, since particles in the PBL was mostly influenced by emissions near the ground. It was found that on non-holidays and holidays* ~~the makeup~~contributions of potential sources ~~was~~ were close to that during the whole Period II, while religious burning contributed about 45% on holiday mornings and exceeded the other two factors. However, the relative relationship of the two factors other

than religious burning was similar under both conditions, with the contribution by combustion/secondary formation nearly 40%

405 of the contribution by dust suspension, suggesting these two sources stayed relatively stable during the campaign. An examination on contributions from the three factors at different time periods on non-holidays revealed the predominant contribution by dust suspension and no obvious diurnal variation of the makeup of potential sources was found. Unlike in the PBL and the RL where the significant importance of coarse mode particles was found, the contribution by large particles that were possibly associated with dust suspension was below 10% in the FT. Factor 1 and 2 contributed approximately 40% and

410 50% in the FT. Although factor 2 was identified as a religious burning factor for the PBL and the RL, this might not be the case in the FT, as the contribution from factor 2 did not differ so much on holiday mornings and at other times. Given the FT was generally much less influenced by emissions near the ground, factor 1 and 2 may be related more to secondary aerosol formation and the aging of existed particles. Measurements of aerosol chemical compositions along the vertical direction in the future might help disentangle this issue.

415 **4 Summary**

In this study, vertical profiles of particle size distributions within 1 km were measured by a POPS and a GRIMM 11-C attached to a tethered balloon in summer 2020 at a suburban site in Lhasa. The variability in the vertical structure and temporal features of parameters such as aerosol number and mass concentrations, the effective diameter and particle mass size distributions were examined. Possible sources for aerosols in different layers were investigated by the PMF analysis.

420 The vertical distribution of aerosol properties was found to be largely governed by the diurnal variation of the boundary layer. Generally speaking, aerosols uniformly distributed in the daytime PBL and sharply declined in the NBL. Usually average particle number and mass concentrations in the FT were less than 25% of the amount in the PBL. For the humid Period I under the influence the Asian Summer Monsoon, a lower level of aerosols and also less large particles in the PBL were found than

that in the relatively dry Period II, possibly due to frequent rainfalls and associated efficient removal by wind. More emissions

425 from religious activities in Period II might also contribute to the differences between the two periods. In contrast, both the total

amount and the size distribution of particle mass in the FT for the two periods were comparable. Residual layers with elevated

aerosol were often encountered in Period II, with particle mass concentrations averagely around 55% of that in the PBL. The

PMSDs in the RL shared a similar pattern as that in the PBL, suggesting they were probably of the same origin. The source

apportionment analysis revealed that the factor associated with suspended dust in the coarse mode contributed more than 50%

430 for the PBL and the RL. However, a distinct peak over 0.5~0.7 μm was observed on religious holiday mornings, the same time

periods when the contribution by the identified religious burning factor with a broad peak over about 0.3~0.7 μm was found

to exceed the contribution by dust suspension. In the FT, submicron particles dominated and the contribution by coarse mode

particles was below 10%. More investigations based on ground-level long-term monitoring and vertical measurements of

aerosol chemical and physical properties will help better identify the origin and evolution processes of aerosols in this area.

435 **Data availability**

~~All data presented in this paper can be accessed by contacting corresponding authors, Zhaoze Deng (dengzz@mail.iap.ac.cn) and Liang Ran (shirleyrl@mail.iap.ac.cn).~~The data in this study can be publicly accessed via https://doi.org/10.5281/zenodo.6374312 (Ran et al., 2022).

Author contribution

440 JB and LR proposed the study. LR, ZD and ZB designed and conducted the field campaign. YL participated in the field campaign. LR and ZD processed the data. JL and YW performed the Positive Matrix Factorization modelling. DZ provided

surface meteorological data. LR visualized the data and wrote the manuscript. ZD and YW participated in several discussions and provided valuable suggestions. All authors reviewed the manuscript carefully.

Acknowledgements

445   This research was funded by the second Tibetan Plateau Scientific Expedition and Research Program (2019QZKK0604). This research was also supported by National Natural Science Foundation of China (NSFC) under grant no. 91837311 and 42061134012. We are grateful to Yong Wang, Hanze Yu and Qi Li for their assistance in launching the tethered balloon. We also thank Tibet University for providing the location for the campaign and all the support.

References

450   Amato, F., Pandolfi, M., Escrig. A., Querol, X., Alastuey, A., Pey, J., Perez, N., and Hopke, P. K.: Quantifying road dust resuspension in urban environment by Multilinear Engine: A comparison with PMF2, Atmos. Environ., 43, 2770-2780, doi:10.1016/j.atmosenv.2009.02.039, 2009.

Atkinson, R.: Atmospheric chemistry of VOCs and NOx, Atmos. Environ., 34, 2063-2101, doi:10.1016/S1352-2310(99)00460-4, 2000.

455   Bai, Y. B., Shi, G. Y., Tamura, K., Shibata, T., Iwasaka, Y., Shin'ichi, K., and Tamio, T.: Aerosol optical properties derived from simultaneous sunphotometer and aureolemeter measurements in Lhasa, J. Environ. Sci., 12, 439-443, 2000.

Brown, S. G., Eberly, S., Paatero, P., and Norris, G. A.: Methods for estimating uncertainty in PMF solutions: Examples with ambient air and water quality data and guidance on reporting PMF results, Sci. Tot. Environ., 518-519, 626-635, doi:10.1016/j.scitotenv.2015.01.022, 2015.

460 Cai, Z. X., Li, Z. Q., L, P. R., Li, J. X., Sun, H. P., Yang, Y. M., Gao, X., Ren, G., Ren, R. M., and Wei, J.: Vertical distributions of aerosol microphysical and optical properties based on aircraft measurements made over the Loess Plateau in China, Atmos. Environ., ~~in press~~270, 118888, doi:10.1016/j.atmosenv.2021.118888, ~~2021~~2022.

Chen, P. F., Kang, S. C., Li, C. L., Li, Q. L., Yan, F. P., Guo, J. M., Ji, Z. M., Zhang, Q. G., Hu, Z. F., Tripathee, L., and Sillanpää, M.: Source apportionment and risk assessment of atmospheric polycyclic aromatic hydrocarbons in Lhasa, Tibet,

465 China, Aerosol Air Qual. Res., 18, 1294-1304, doi:10.4209/aaqr.2017.12.0603, 2018.

Chiang, J. C. H., Kong, W., Wu, C. H., and Battisti, D. S.: Origins of East Asian Summer Monsoon seasonality, J. Climate, 33, 7945-7965, doi: 10.1175/JCLI-D-19-0888.1, 2020.

Cong, Z. Y., Kang, S. C., Luo, C. L., Li, Q., Huang, J., Gao, S. P., and Li, X. D.: Trace elements and lead isotopic composition of PM_{10} in Lhasa, Tibet, Atmos. Environ., 45, 6210-6215, doi:10.1016/j.atmosenv.2011.07.060, 2011.

470 Cui, L. L., Duo, B., Zhang, F., Li, C. L., Fu, H. B., and Chen, J. M.: Physiochemical characteristics of aerosol particles collected from the Jokhang Temple indoors and the implication to human exposure, Environ. Pollut., 236, 992-1003, doi: 10.1016/j.envpol.2017.10.107, 2018a.

Cui, Y. Y., Liu, S., Bai, Z. X., Bian, J. C., Li, D., Fan, K. Y., McKeen, S. A., Watts, L. A., Ciciora, S. J., and Gao, R. S.: Religious burning as a potential major source of atmospheric fine aerosols in summertime Lhasa on the Tibetan Plateau, Atmos.

475 Environ., 181, 186-191, doi:10.1016/j.atmosenv.2018.03.025, 2018b.

Ding, Y. H.: The variability of the Asian Summer Monsoon, J. Meteor. Soc. Japan, 85B, 21-54, doi:10.2151/jmsj.85B.21, 2007.

Duo, B., Zhang, Y. C., Kong, L. D., Fu, H. B., Hu, Y. J., Chen, J. M., Li, L., and Qiong, A.: Individual particle analysis of aerosols collected at Lhasa City in the Tibetan Plateau, J. Environ. Sci., 29, 165-177, doi:10.1016/j.jes.2014.07.032, 2015.

480 Duo, B., Cui, L. L., Wang, Z. Z., Li, R., Zhang, L. W., Fu, H. B., Chen, J. M., Zhang, H. F., and Qiong, A.: Observations of atmospheric pollutants at Lhasa during 2014-2015: Pollution status and the influence of meteorological factors, J. Environ. Sci., 63, 28-42, doi:10.1016/j.jes.2017.03.010, 2018.

Ferrero, L., Perrone, M. G., Petraccone, S., Sangiorgi, G., Ferrini, B. S., Lo Porto, C., Lazzati, Z., Cocchi, D., Bruno, F., Greco, F., Riccio, A., and Bolzacchini, E.: Vertically-resolved particle size distribution within and above the mixing layer over the

485 Milan metropolitan area, Atmos. Chem. Phys., 10, 3915-3932, doi:10.5194/acp-10-3915-2010, 2010.

Ferrero, L., Castelli, M., Ferrini, B. S., Moscatelli, M., Perrone, M. G., Sangiorgi, G., D'Angelo, L., Rovelli, G., Moroni, B., Scardazza, F., Mocnik, G., Bolzacchini, E., Petitta, M., and Cappelletti, D.: Impact of black carbon aerosol over Italian basin valleys: high-resolution measurements along vertical profiles, radiative forcing and heating rate, Atmos. Chem. Phys., 14, 9641-9664, doi:10.5194/acp-14-9641-2014, 2014.

490 Gao, R. S., Telg, H., McLaughlin, R. J., Ciciora, S. J., Watts, L. A., Richardson, M. S., Schwarz, J. P., Perring, A. E., Thornberry, T. D., Rollins, A. W., Markovic, M. Z., Bates, T. S., Johnson, J. E., and Fahey, D. W.: A light-weight, high-sensitivity particle spectrometer for $PM_{2.5}$ aerosol measurements, Aerosol Sci. Technol., 50, 88-99, doi: 10.1080/02786826.2015.1131809, 2016.

Gong, P., Wang, X. P., and Yao. T. D.: Ambient distribution of particulate- and gas-phase n-alkanes and polycyclic aromatic

495 hydrocarbons in the Tibetan Plateau, Environ. Earth Sci., 64, 1703-1711, doi:10.1007/s12665-011-0974-3, 2011.

He, C., Wang, Z. Q., Zhou, T. J., and Li, T.: Enhanced latent heating over the Tibetan Plateau as a key to the enhanced East Asian Summer Monsoon circulation under a warming climate, J. Climate, 32, 3373-3388, doi:10.1175/JCLI-D-18-0427.1, 2019.

Jarvis, A., Reuter, H. I., Nelson, A., and Guevara, E.: Hole-filled seamless SRTM data V4, International Centre for Tropical

500 Agriculture (CIAT), available from http://srtm.csi.cgiar.org, 2008.

Juntto, S. and Paatero, P.: Analysis of daily precipitation data by positive matrix factorization, Environmetrics, 5, 127-144, doi:10.1002/env.3170050204, 1994.

Kim, S. W., Yoon, S. C., Won, J. G., and Choi, S. C.: Ground-based remote sensing measurements of aerosol and ozone in an urban area: a case study of mixing height evolution and its effect on ground-level ozone concentrations, Atmos. Environ., 41, 505 7069-7081, doi:10.1016/j.atmosenv.2007.04.063, 2007.

Li, C. L., Han, X. W., Kang, S. C., Yan, F. P., Chen, P. F., Hu, Z. F., Yang, J. H., Ciren, D. J., Gao, S. P., Sillanpää, M., Han, Y. M., Cui, Y. Y., Liu, S., and Smith, K. R.: Heavy near-surface $PM_{2.5}$ pollution in Lhasa, China during a relatively static winter period, Chemosphere, 214, 314-318, doi:10.1016/j.chemosphere.2018.09.135, 2019.

Lin, W., Zhu, T., Song, Y., Zou, H., Tang, M., Tang, X., and Hu, J.: Photolysis of surface O_3 and production potential of OH 510 radicals in the atmosphere over the Tibetan Plateau, J. Geophys. Res., 113, D02309, doi:10.1029/2007JD008831, 2008.

Liu, J. W., Li, J., Lin, T., Liu, D., Xu, Y., Chaemfa, C., Qi, S. H., Liu, F. B., and Zhang, G.: Diurnal and nocturnal variations of PAHs in the Lhasa atmosphere, Tibetan Plateau: Implication for local sources and the impact of atmospheric degradation processing, Atmos. Res., 124, 34-43, doi:10.1016/j.atmosres.2012.12.016, 2013.

Liu, P. F., Zhao, C. S., Zhang, Q., Deng, Z. Z., Huang, M. Y., Ma, X. C., and Tie, X. X.: Aircraft study of aerosol vertical 515 distributions over Beijing and their optical properties, Tellus, 61B, 756-767, doi:10.1111/j.1600-0889.2009.00440.x, 2009.

Paatero, P.: Least squares formulation of robust non-negative factor analysis, Chemom. Intell. Lab. Syst., 37, 23-35, doi: 10.1016/S0169-7439(96)00044-5, 1997.

Paatero, P. and Hopke, P. K.: Discarding or downweighting high-noise variables in factor analytic models, Anal. Chim. Acta, 490, 277-289, doi:10.1016/S0003-2670(02)01643-4, 2003.

520 Paatero, P. and Tapper, U.: Positive matrix factorization: A non-negative factor model with optimal utilization of error estimates of data values, Environmetrics, 5, 111-126, doi:10.1002/env.3170050203, 1994.

Ran, L., Lin, W., Deji, Y., La, B., Tsering, P., Xu, X., and Wang, W.: Surface gas pollutants in Lhasa, a highland city of Tibet - current levels and pollution implications, Atmos. Chem. Phys., 14, 10721-10730, doi:10.5194/acp-14-10721-2014, 2014.

Ran, L., Deng, Z. Z., Xu, X. B., Yan, P., Lin, W. L., Wang, Y., Tian, P., Wang, P. C., Pan, W. L., and Lu, D. R.: Vertical

525   profiles of black carbon measured by a micro-aethalometer in summer in the North China Plain, Atmos. Chem. Phys., 16, 10441-10454, doi:10.5194/acp-16-10441-2016, 2016.

Seibert, P., Beyrich, F., Gryning, S. E., Joffre, S., Rasmussen, A., and Tercier, P.: Review and intercomparison of operational methods for the determination of the mixing height, Atmos. Environ., 34, 1001-1027, doi:10.1016/S1352-2310(99)00349-0, 2000.

530   Shingler, T., Crosbie, E., Ortega, A., Shiraiwa, M., Zuend, A., Beyersdorf, A., Ziemba, L., Anderson, B., Thornhill, L., Perring, A. E., Schwarz, J. P., Campazano-Jost, P., Day, D. A., Jimenez, J. L., Hair, J. W., Mikoviny, T., Wisthaler, A., and Sorooshian, A.: Airborne characterization of subsaturated aerosol hygroscopicity and dry refractive index from the surface to 6.5 km during the SEAC4RS campaign, J. Geophys. Res. Atmos., 121, 4188-4210, doi:10.1002/2015JD024498, 2016.

535   Sloane, C. S., Watson, J., Chow, J., Pritchett, L., and Richards, L. W.: Size-segregated fine particle measurements by chemical species and their impact on visibility impairment in Denver, Atmos. Environ., 25, 1013-1024, doi:10.1016/0960-1686(91)90143-U, 1991.

Tao, J., Zhang, L. M., Cao, J. J., Hsu, S.-C., Xia, X. A., Zhang, Z. S., Lin, Z. J., Cheng, T. T., and Zhang, R. J.: Characterization and source apportionment of aerosol light extinction in Chengdu, southwest China, Atmos. Environ., 95, 552-562,

540   doi:10.1016/j.atmosenv.2014.07.017, 2014.

Tobo, Y., Iwasaka, Y., Shi, G. Y., Kim, Y. S., Ohashi, T., Tamura, K., and Zhang, D. Z.: Balloon-borne observations of high aerosol concentrations near the summertime tropopause over the Tibetan Plateau, Atmos. Res., 84, 233-241, doi: 10.1016/j.atmosres.2006.08.003, 2007.

Wan, X., Kang, S. C., Xin, J. Y., Liu, B., Wen, T. X., Wang, P. L., Wang, Y. S., and Cong, Z. Y.: Chemical composition of
545   size-segregated aerosols in Lhasa city, Tibetan Plateau, Atmos. Res., 174-175, 142-150, doi: 10.1016/j.atmosres.2016.02.005, 2016.

Wei, N. N., Ma, C. L., Liu, J. W., Wang, G. H., Liu, W., Zhuoga, D. Q., Xiao, D. T., and Yao, J.: Size-segregated characteristics of carbonaceous aerosols during the monsoon and non-monsoon seasons in Lhasa in the Tibetan Plateau, Atmosphere, 10, 157, doi:10.3390/atmos10030157, 2019a.

550   Wei, N. N., Xu, Z. Y., Liu, J. W., Wang, G. H., Liu, W., Zhuoga, D. Q., Xiao, D. T., and Yao, J.: Characteristics of size distributions and sources of water-soluble ions in Lhasa during monsoon and non-monsoon seasons, J. Environ. Sci., 82, 155-168, doi:10.1016/j.jes.2019.02.017, 2019b.

Yin, X. F., de Foy, B., Wu, K. P., Feng, C., Kang, S. C., and Zhang, Q. G.: Gaseous and particulate pollutants in Lhasa, Tibet during 2013-2017: Spatial variability, temporal variations and implications, Environ. Pollut., 253, 68-77, doi:
555   10.1016/j.envpol.2019.06.113, 2019.

Zhang, D. Z., Iwasaka, Y., and Shi, G. Y.: Soot particles and their impacts on the mass cycle in the Tibetan atmosphere, Atmos. Environ., 35, 5883-5894, doi:10.1016/S1352-2310(01)00391-0, 2001a.

Zhang, K., Wang, D. F., Bian, Q. G., Duan, Y. S., Zhao, M. F., Fei, D. N., Xiu, G. L., and Fu, Q. Y.: Tethered balloon-based particle number concentration, and size distribution vertical profiles within the lower troposphere of Shanghai, Atmos.
560   Environ., 154, 141-150, doi:10.1016/j.atmosenv.2017.01.025, 2017.

Zhang, X. Y., Arimoto, R., Cao, J. J., An, Z. S., and Wang, D.: Atmospheric dust aerosol over the Tibetan Plateau, J. Geophys. Res., 106, 18471-18476, doi:10.1029/2000JD900672, 2001b.

Zhang, Y. L., Li, B. Y., Liu, L. S., Zheng, D.: Redetermine the region and boundaries of Tibetan Plateau, Geograph. Res., 40, 1543-1553, doi:10.11821/dlyj020210138, 2021. (in Chinese)

565   Zhu, C. S., Cao, J. J., Hu, T. F., Shen, Z. X., Tie, X. X., Huang H., Wang, Q. Y., Huang, R. J., Zhao, Z. Z., Močnik, G., and Hansen, A. D. A.: Spectral dependence of aerosol light absorption at an urban and a remote site over the Tibetan Plateau, Sci. Total Environ., 590-591, 14-21, doi:10.1016/j.scitotenv.2017.03.057, 2017.

Zhu, J., Xia, X. A., Che, H. Z., Wang, J., Cong, Z. Y., Zhao, T. L., Kang, S. C. Zhang, X. L., Yu, X. N., and Zhang, Y. L.: Spatiotemporal variation of aerosol and potential long-range transport impact over the Tibetan Plateau, China, Atmos. Chem.

570   Phys., 19, 14637-14656, doi:10.5194/acp-19-14637-2019, 2019.